PG
Petroleum Geoscience

Research article

Published online July 12, 2016 doi:10.1144/petgeo2016-036 | Vol. 22 | 2016 | pp. 211–222

Carbon dioxide storage in the Captain Sandstone aquifer: determination of *in situ* stresses and fault-stability analysis

John D. O. Williams[1*], Mark W. Fellgett[1] & Martyn F. Quinn[2]

[1] British Geological Survey, Environmental Science Centre, Keyworth, Nottingham NG12 5GG, UK
[2] British Geological Survey, The Lyell Centre, Research Avenue South, Edinburgh EH14 4AP, UK
* Correspondence: jdow@bgs.ac.uk

Abstract: The Lower Cretaceous Captain Sandstone Member of the Inner Moray Firth has significant potential for the injection and storage of anthropogenic CO_2 in saline aquifer parts of the formation. Pre-existing faults constitute a potential risk to storage security owing to the elevated pore pressures likely to result from large-scale fluid injection. Determination of the regional *in situ* stresses permits mapping of the stress tensor affecting these faults. Either normal or strike-slip faulting conditions are suggested to be prevalent, with the maximum horizontal stress orientated 33°–213°. Slip-tendency analysis indicates that some fault segments are close to being critically stressed under strike-slip stress conditions, with small pore-pressure perturbations of approximately 1.5 MPa potentially causing reactivation of those faults. Greater pore-pressure increases of approximately 5 MPa would be required to reactivate optimally orientated faults under normal faulting or transitional normal/strike-slip faulting conditions at average reservoir depths. The results provide a useful indication of the fault geometries most susceptible to reactivation under current stress conditions. To account for uncertainty in principal stress magnitudes, high differential stresses have been assumed, providing conservative fault-stability estimates. Detailed geological models and data pertaining to pore pressure, rock mechanics and stress will be required to more accurately investigate fault stability.

Received 18 February 2016; **revised** 13 May 2016; **accepted** 25 May 2016

Large-scale deployment of CO_2 storage as a strategy for reducing greenhouse gas emissions will rely on the integrity of sealing strata overlying the storage reservoirs to ensure that the captured CO_2 is permanently isolated from the atmosphere (IPCC 2005; Chadwick *et al.* 2009*a*; Holloway 2009). The existence of pre-existing fault systems of varying dimensions is a common feature throughout the subsurface, and the efficacy of seals may potentially be compromised by any enhanced transmissibility associated with fault zones. Within the Moray Firth, the Lower Cretaceous Captain Sandstone Member of the Wick Sandstone Formation has been proposed as a suitable storage reservoir candidate (SCCS 2011; Shell 2011*a*; Akhurst *et al.* 2015). Storage potential exists within depleting hydrocarbon fields (Marshall *et al.* 2016), while significant additional capacity is available in the surrounding saline aquifer volume. Regional top seals include the Cretaceous Rodby, Carrack and Valhall formations. Simulation studies of CO_2 injection identified the storage capacity of the Captain Sandstone to be between 358 and 2495 Mt (Jin *et al.* 2012). As the injection of CO_2 is reliant on the displacement of existing pore fluids, large-scale injection results in increased pore-fluid pressure, the effects of which will be felt across large areas in well-connected aquifer systems (Chadwick *et al.* 2009*b*; Jin *et al.* 2012; Noy *et al.* 2012).

It is well documented that some faults are transmissible to fluid flow, while others act as effective capillary seals (Caine *et al.* 1996; Aydin 2000; Faulkner *et al.* 2010). Whether cross-fault flow occurs depends on the juxtaposition of lithologies in the footwall and hanging-wall blocks, as well as the composition of the fault zone and any differential pressure across the fault. In addition, reactivation of previously stable faults caused by increasing pressure, and therefore a reduction in the effective stress, could allow faults to become transmissive to buoyant fluids, such as supercritical CO_2, due to the opening of flow pathways during failure (Streit & Hillis 2004). It is this aspect of fault stability that forms the focus of this study, with respect to the Captain Sandstone of the Inner Moray Firth, and utilizing an adaptation of the geological model presented by Jin *et al.* (2012).

Analysis of the geomechanical stability of faults offsetting the Captain Sandstone requires the contemporary stress field affecting the basin to be characterized, in order to resolve the shear and normal stresses acting on mapped faults and to determine which faults, or segments of faults, are most susceptible to becoming reactivated if pore-fluid pressures in the basin are increased as a result of CO_2 injection. In order to do so, detailed knowledge of the pore-pressure conditions at depth, the magnitude and orientations of the principal stresses, and the properties of the faults is required.

Geological setting

The Captain Sandstone is located within the eastern part of the Inner Moray Firth (IMF), and the western part of the Outer Moray Firth (OMF) basins (Fig. 1). In general, the present-day geological structure of the Moray Firth region is characterized by ENE–WSW-trending fault-defined horsts, basins and sub-basins formed from a series of Mesozoic displacements. The IMF has a dominantly NE structural trend, while the OMF has a predominantly NW structural trend. Subsequent reactivation of some of the faults during the Cenozoic resulted in some fault displacements propagating to the seabed. The ENE-trending Wick Fault Zone marks the northern boundary of the present study area. The Smith Bank (ENE-trending), West Halibut (east–west- to NW–SE-trending) and the Little Halibut (NW-trending) faults mark the boundaries of the Halibut Horst, a major Jurassic structural high that lies beneath the southern part of the study area. The Halibut Horst was present throughout the Lower Cretaceous where it influenced sedimentation patterns of the deep submarine fans that include the Captain sandstone; the horst was eventually submerged during the Late Cretaceous (Ahmadi *et al.* 2003).

A major rifting event, spanning Late Jurassic–Early Cretaceous times, comprising faulting episodes interspersed by periods of

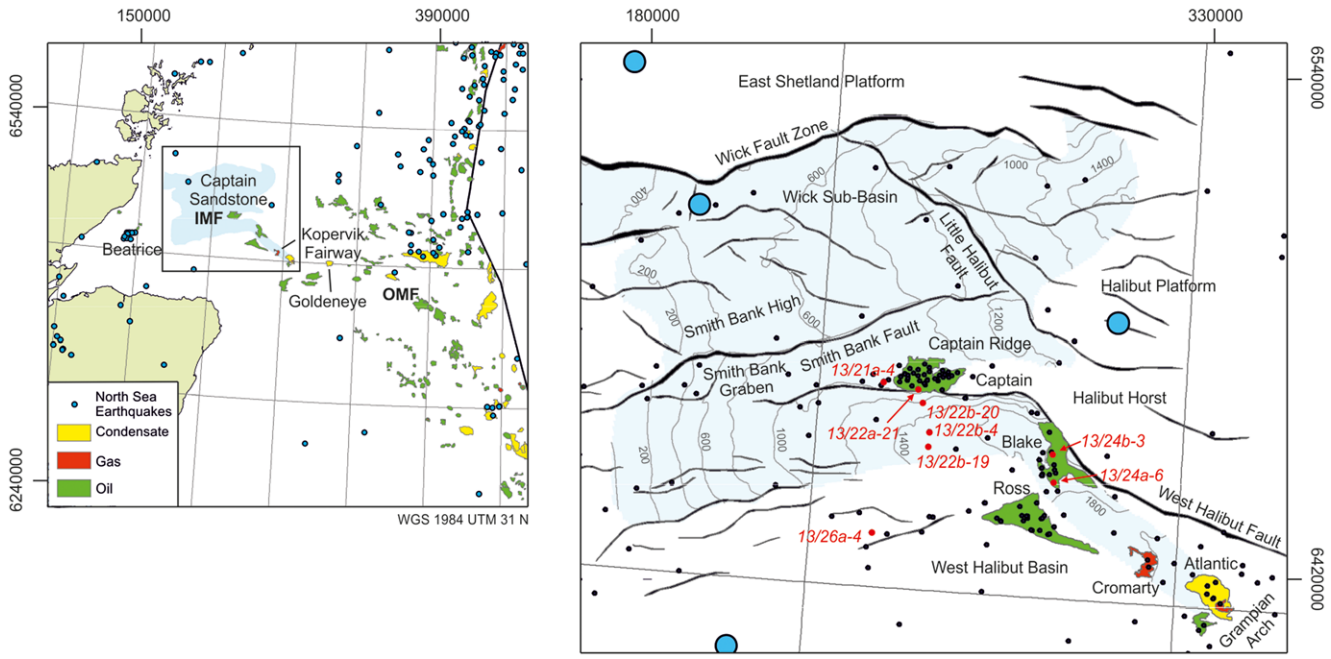

Fig. 1. Location of the study area, main geological features relevant to this study (IMF and OMF, Inner and Outer Moray Firth, respectively), wells (small dots, wells used in the study are labelled) and the British Geological Survey (BGS) seismicity catalogue up to 2012 (filled circles). Fault locations shown for the base Cretaceous and top Captain Sandstone depth contours (metres relative to the seabed) were derived from SCCS (2011). Note the Kopervik Fairway is known to extend further eastwards than shown (Law *et al.* 2000; Marshall *et al.* 2016). Offshore quadrant and field linework contain public sector information licenced under the Open Government Licence v3.0.

relative tectonic quiescence, resulted in the development of numerous half-graben and associated synrift deposits over the area (Hillis *et al.* 1994; Zanella & Coward 2003). The regional extension direction during this time was NE–SW, resulting in the formation of new NW-trending normal faults or reactivation of existing faults with normal or strike-slip components depending on their orientation: for instance, existing ENE-trending faults might have been reactivated with a strike-slip component (Zanella & Coward 2003). The progressive onlap shown by Lower Cretaceous shales and sands onto basin margins and of the Upper Cretaceous Chalk onto basin highs is interpreted as evidence of a post-rift thermal phase of subsidence, with the sedimentary environment in this area set against a background of rising sea level (Hillis *et al.* 1994). However, during the Lower Cretaceous, this general increase in sea level was punctuated by sea-level falls during the Hauterivian–Valanginian and later during the Aptian times, related to far-field tectonic events (Oakman 2005). These periods of lowered sea level exposed shelf areas and caused sand, originally sourced from north and west of the Wick Fault Zone, to be deposited in deeper water by gravity-flow processes feeding submarine fans that led to the accumulation of the Wick Sandstone Formation (Fig. 2) (Johnson & Lott 1993). The half-graben topography played an important role in the distribution of Lower Cretaceous sandstones in these basins (Rose *et al.* 2000). Deposition of the Late Cretaceous

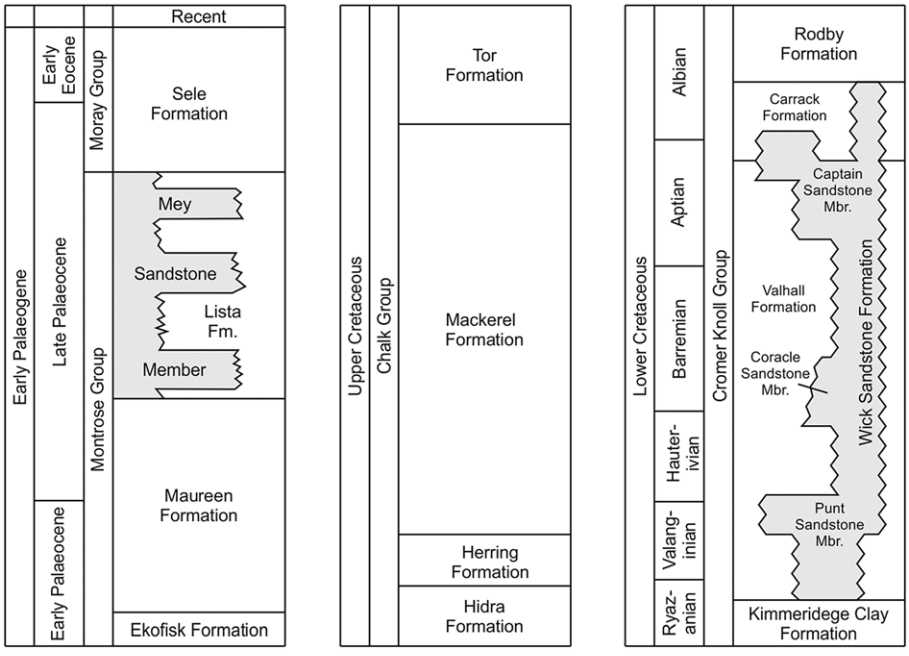

Fig. 2. Lithostratigraphy of the Inner Moray Firth after Johnson & Lott (1993). Significant sandstone bodies are highlighted grey.

Chalk Group reflects the widespread flooding of the basin/high topography during a time of relative tectonic quiescence but punctuated by pulses of compression related to the Alpine Orogeny, although in the study area the effects are thought to be quite weak (Zanella & Coward 2003). Regional uplift of the Scottish Highlands and East Shetland Platform at the beginning of the Paleocene led to the deposition of large volumes of siliciclastic sediments (Ahmadi *et al.* 2003). In the study area, a shelf-environment setting prevailed with deposition characterized by transgression and restricted deposition along basin margins or regression leading to more widespread gravity-flow deposition into the basin itself (Garrett *et al.* 2000; Ahmadi *et al.* 2003). It is generally accepted that the subcrop of Mesozoic and Cenozoic rocks at the seabed in the Inner Moray Firth is the result of Cenozoic uplift (Argent *et al.* 2002), and Hillis *et al.* (1994) suggested significant uplift and erosion during the Danian. Cenozoic uplift led to the reactivation of earlier faults, some of which have propagated to the seabed. However, Richardson *et al.* (2005) noted that the main bounding fault of the Beatrice Field had not propagated to the seabed and remained as a seal for the trapped hydrocarbons.

Over the study area, the post-Jurassic succession comprises Paleocene, Upper Cretaceous Chalk and Lower Cretaceous Cromer Knoll groups that shallow and progressively subcrop the seabed towards the coast (Fig. 1). The Lower Cretaceous Cromer Knoll Group generally rests conformably on Upper Jurassic sediments over much of the area (Thomson & Underhill 1993) and reaches thicknesses of more than 1000 m to the NW, adjacent to the Wick Fault Zone (Copestake *et al.* 2003), but thins and onlaps the Captain Ridge and Halibut Horst (Rose 1999). In some areas, the Lower Cretaceous and underlying Jurassic are absent, and Upper Cretaceous Chalk rests unconformably on Devonian Old Red Sandstone. The Upper Cretaceous Chalk varies in thickness from 250 to 500 m, and reaches over 750 m south of the Wick Fault Zone. It is absent along the western margin of the model due to erosion (Surlyk *et al.* 2003) and here the underlying Lower Cretaceous stratigraphy subcrops at the seabed (Fig. 1). The Paleocene is also absent along the western margin of the model, but thickens rapidly to more than 900 m on the southern side of the Halibut Horst, and varies between 200 and 750 m over much of the study area (Ahmadi *et al.* 2003).

The Lower Cretaceous Cromer Knoll Group (Fig. 2) (Johnson & Lott 1993) comprises the Rodby, Carrack, Valhall and Wick formations. The Lower Cretaceous Wick Sandstone Formation comprises laterally extensive units of occasionally thick sandstone interbedded with siltstone and mudstone that are interpreted as having been deposited by a range of mass-flow processes (Fig. 2) (Johnson & Lott 1993). The Wick Sandstone Formation has been divided into three members: the Captain Sandstone (Early Aptian–earliest Albian) is the youngest of three members, the others being the Coracle (latest Early Hauterivian–earliest Barremian) and the Punt (intra-Late Ryazanian–earliest Hauterivian). Because there are fewer well penetrations at depth, the older members are poorly resolved on seismic data, and the extent and disposition of the Coracle and Punt sandstones is not well known. The Wick Sandstone Formation passes laterally into the dominantly mud-prone successions of the Valhall Formation, which comprises interbedded calcareous mudstone and thin limestone, and the Carrack Formation that comprises non-calcareous, carbonaceous, pyritic, micaceous mudstone and siltstone: both of these formations may also locally contain mass-flow sandstone and occasional conglomerate (Johnson & Lott 1993). The overlying Rodby Formation comprises calcareous mudstone with occasional thin beds of argillaceous limestone.

Geological model location and context

Hydrocarbons are produced from the Captain Sandstone in several fields, notably the Captain and Blake oil fields, the Cromarty Gas Field, and the Atlantic and Goldeneye gas condensate fields. The Wick Fault Zone forms the northern boundary to the Captain Sandstone, while faulting and stratigraphic closure form the southern boundary. With the exception of the Captain Oil Field, which is situated on the Captain Ridge to the west of the Halibut Horst, the other fields are located along a thin sand-rich pan-handle termed the Kopervik Fairway (Law *et al.* 2000) that extends eastwards along strike of the South Halibut Trough. The depleted Goldeneye Field has been proposed as a site for the storage of CO_2 (Shell 2011*a*; Marshall *et al.* 2016): however, the present study focuses on the main depocentre to the West of the Halibut Horst, corresponding roughly to the Wick Sub-basin, the Smith Bank High and the Smith Bank Graben, where a pre-existing 3D geological model is available. The model does not extend eastwards beyond the Atlantic Field in the vicinity of the Grampian Arch, and so does not include the full length of the Kopervik Fairway (Fig. 1). The model comprises the Captain Sandstone aquifer and its under- and overburden, and has been adapted from interpretations used to generate the reservoir simulation model of Jin *et al.* (2012), based on interpretation of 2D seismic reflection and well data. The data and methodology that contributed towards the geometry and structure of the original model is described in a research report (Quinn *et al.* 2010), and is not described in detail here.

Unlike the proposed Goldeneye storage site, in this area there are no specific structural traps that have been specifically identified for CO_2 storage, so any prospective projects would need to take measures to avoid the updip migration of CO_2 towards shallower depths and, ultimately, towards the seabed. Jin *et al.* (2012) conducted multiphase fluid-flow simulations which demonstrated that storage capacities in excess of 1 Gt could be achieved without CO_2 reaching a depth significantly shallow so as not to exist in a supercritical state, limiting the risk of westwards migration towards the seabed. Water depth across the study area is in the range of 30–120 m, with an average of 90 m.

In the adapted model used here, faulting has been restricted to those faults that affect the Captain Sandstone reservoir and its overburden only, as these are the faults most likely to experience increased pressure during injection and to pose a risk to storage integrity. Deeper faults that do not cut the Captain Sandstone or its overburden would not be expected to experience significant increased pore-pressure perturbations as a result of injection, so reactivation of these faults, although possible, is not considered a risk to storage integrity despite the potential for induced seismicity. The number of faults within the model was therefore reduced from 43 to 15. It is noted that unmapped or non-seismically resolvable faults are also likely to be present across the study region given that no 3D seismic reflection data were available to the mapping exercise. The potential presence of such faults should also be considered in studies of regional geomechanical stability.

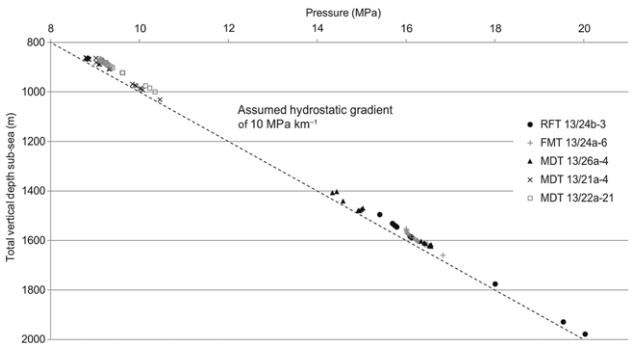

Fig. 3. Pressure measurements and hydrostatic gradient to surface across the Captain Sandstone. Location of the wells shown in Figure 1.

Table 1. *Summary of wellbore breakouts interpreted from image logs. The mean and standard deviation have been calculated using the directional statistics of Mardia (1972). Image logs for well 13/24a-6 were not reinterpreted as part of this study*

Well name	Image type	Start depth (m)	Number of breakouts	Total length (m)	S_{Hmax} azimuth	Standard deviation	WSM rank
13/21a–4	FMI	937	1	0.73	30	–	D
13/24b–3	UBI	1590	4	2.9	42	12	D
13/26a–4	FMI	1021	10	8.15	29	6	D
13/24a–6	*STAR*	–	*27*	–	*33*	–	–
Combined (this analysis)	–	937–1590 (range)	15	11.78	33	9	D

As shown by Figure 1, the area is relatively aseismic, with the exception of a series of seismic events clustered around the Beatrice Oil Field. Although the co-location of the seismicity in relation to the field boundaries suggest that they may be related to petroleum production, Wilson *et al.* (2015) curiously observed little correlation in relation to the production and injection history of the field.

Determination of the stress field

In order to examine the stability of faults in the current stress regime, and to quantify the effects of increasing pore-fluid pressures, it is necessary to consider the 3D geometry of the faults, and to understand the orientations and magnitudes of the three principal stresses. Such information is either directly measureable or can be inferred from data acquired in hydrocarbon wells. In this section, the characteristics of the stress field affecting the Cretaceous and younger strata are derived from hydrocarbon well data.

Pore-fluid pressure

Direct measurements of pore-fluid pressure over the Lower Cretaceous are available from several hydrocarbon wells across the study region. Repeat Formation Tester (RFT), Modular Formation Dynamics Tester (MDT) and Formation Multi Tester (FMT) data provide pressure measurements over the Captain, Coracle and Ettrick sandstones, and record a pore-fluid pressure gradient of approximately 0.01 MPa m^{-1} (Fig. 3). A similar pore-pressure gradient is seen in the Jurassic Claymore and Ross Sandstone members in well 13/26a-4. The pore-pressure measurements are slightly above an assumed hydrostatic gradient of 10 MPa km^{-1} from the surface level, but as the Lower Cretaceous penetrated by these wells contains hydrocarbons, and given the lack of information regarding brine salinity variations with depth, a pore-pressure gradient of 10 MPa km^{-1} to the surface is assumed over the wider area. Despite the history of oil and gas production from the Captain Sandstone, widespread pressure depletion of the reservoir pore pressure is unlikely in the area west of the Kopervik Fairway due to pressure maintenance in the Captain and Blake oil fields (Du *et al.* 2000; Pinnock & Clitheroe 2003). Owing to the good fit of the assumed gradient to the observed data, the variation in the pore-pressure gradient is expected to be small and should not significantly affect the results of the fault-stability analysis.

Stress orientations

The vertical stress (S_v) is generally considered to be one of the principal stresses in the subsurface, while the other two principal stresses are horizontal and orthogonal to each other. Borehole breakout and drilling-induced tensile fracture are modes of borehole failure resulting from stress concentration in the rock around a wellbore once the material supporting that rock is removed (Zoback *et al.* 1985; Bell 1990). Breakouts are enlargements of the borehole wall formed by the development of conjugate shear fractures, while drilling-induced tensile fractures develop as narrow features sub-parallel to the borehole axis in vertical wells and are not associated with significant borehole enlargement. In approximately vertical boreholes, such as those studied here, breakouts occur in the direction of the minimum horizontal stress (S_{hmin}) and therefore the borehole is enlarged in a direction perpendicular to the maximum horizontal stress (S_{Hmax}), while drilling-induced tensile fractures strike in the direction of S_{Hmax} (Plumb & Hickman 1985; Aadnoy & Bell 1998).

Downhole ultrasonic televiewer and electrical borehole image logs provide a means by which to interpret the presence or absence of both borehole breakouts and drilling-induced tensile fractures, and therefore to determine the orientations of the horizontal principal stresses over the logged intervals. Ultrasonic borehole image (UBI) log data are available for the 13/24b–3 well, and Formation Micro Imager (FMI) logs are available for three other wells in the area, enabling an analysis of the stress orientations in the region. While no drilling-induced tensile fractures were observed from any of the logs, several breakouts are observed in three of the wells (Table 1). No reliable breakouts were detected in well 13/22a-21, possibly due to the limited borehole coverage imaged by the logs in this well. As such, it is not possible to determine that borehole breakouts are absent in this well, only that they are not detected using the logs available. Four discrete breakouts were observed in well 13/24b-3, examples of which are shown in Figure 4. Figure 5 shows examples of observed borehole breakouts from the FMI logs in well 13/26a-4. Although this well lies outside the extent of the Captain Sandstone Member, the FMI log provides some good examples of borehole breakout over the time-equivalent Valhall and Carrack formations.

Borehole breakouts observed from image logs in several wells from the IMF provide information relevant to the determination of stress orientation in the basin (Table 1). The measurements all support a generally NE–SW orientation of S_{Hmax}. The measurements have been subjected to the quality ranking scheme utilized by the World Stress Map (WSM) project (Sperner *et al.* 2003; Heidbach *et al.* 2010). They are considered to represent good

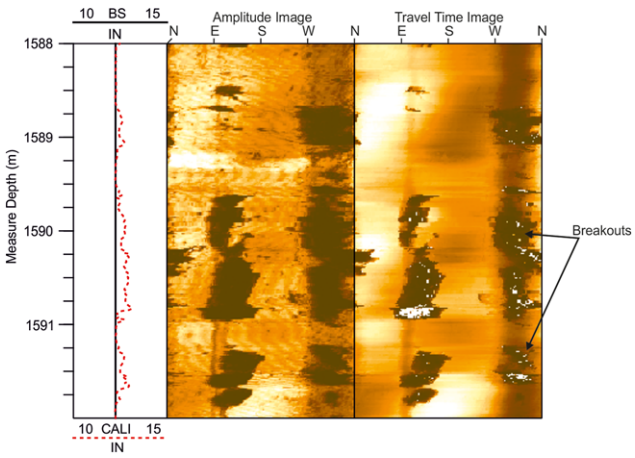

Fig. 4. Example of breakouts from UBI logs in well 13/24b-3. Breakouts are identified by darker zones of increased borehole radius. Note also the borehole enlargement indicated by the caliper log.

measurements of the horizontal stress directions due to the clarity of the processed images: however, these would be classified only as category D measurements according to the WSM ranking scheme. This is due to the limited number of observed breakouts in these wells and to the short combined length (height) of the observed breakouts. As the breakout orientations appear to be consistent across the region, they are considered to be representative of the far-field orientation of S_{Hmax}, so the mean orientation of 33°–213° derived from all breakout orientations using the directional statistics of Mardia (1972) is used in this analysis. The orientations of S_{Hmax} are shown in Figure 6. These observations are consistent with those of 27 breakouts that indicate S_{Hmax} striking in a mean orientation of 33°–213° reported from the Valhall Formation in well 13/24a-6, interpreted from the analysis of Simultaneous Acoustic and Resistivity (STAR) image logs reported by Hilton (1999). Although the STAR image logs have not been reinterpreted for this study, the reported orientation of S_{Hmax} from the well is also shown in Figure 6. Although it is noted that only a limited dataset is available, the mean S_{Hmax} orientation is considered to be reasonably well constrained due to the similarity of orientations at different depths and in each of the studied wells, and due to the low standard deviation of all the breakouts (9.4°). It is not expected that a variation of this amount will be sufficient to significantly affect the fault-stability analysis.

The far-field stresses affecting NW Europe result from the configuration of tectonic plate boundaries and associated ridge-push forces (Gölke & Coblentz 1996): however, the orientations of S_{Hmax} observed from the IMF suggest a departure from the NW–SE orientation expected, which is observed onshore UK (Kingdon *et al.* 2016). This suggests that the structural lineaments bounding the IMF Basin have altered the orientation of the tectonic stresses, a feature of the North Sea stress field previously suggested by Cowgill *et al.* (1993). Permian evaporite sequences are relatively thin and do not impose a control on the Mesozoic–Recent stress regime as they have been proposed to do in the Central and Southern North Sea regions (Hillis & Nelson 2005; Williams *et al.* 2015).

Stress magnitudes

The magnitude of the vertical stress (S_v) was obtained by integrating rock densities from downhole bulk density logs in three wells using equation (1), after Zoback *et al.* (2003):

$$s_v = \rho_w g z_w + \int_{z_w}^{z} \rho(z) g \, dz \approx \rho_w g z_w + \bar{\rho} g (z - z_w) \qquad (1)$$

where $\rho(z)$ is density as a function of depth, g is the acceleration due to gravity, $\bar{\rho}$ is the mean overburden density, ρ_w is the density of water (taken as 1 g cm^{-3}) and z_w is water depth. As the strata in the shallower section were not logged by the density tool (Fig. 7a), an average rock density of 2.5 g cm^{-3} was inferred for the unlogged section up to the seabed. An average overburden stress profile was calculated from the three wells and is shown in Figure 7b. The overburden stress gradient to the seabed can be conveniently expressed as a S_v gradient of 25 MPa km^{-1}. The lack of density logs in the shallower section (Fig. 7a) gives rise to some uncertainty regarding the magnitude of S_v. Bulk density of the relatively less-consolidated Palaeogene in the shallower subsurface is likely to be less than that assumed, and so the calculated overburden stress profile could give rise to slightly elevated S_v magnitudes at depth. This would result in greater differential stress between S_v and the minimum principal stress, resulting in a higher susceptibility of faults to fail. The fault-stability analysis is therefore regarded as conservative.

The magnitude of the least principal stress (fracture pressure) is commonly estimated from leak-off tests (LOTs), during which small-scale hydraulic fracturing occurs. The tests are conducted in short open-hole well sections beneath cemented casing shoes primarily to assess suitable drilling mud densities, but can also be used to determine the magnitude of the least principal stress. Available LOT data for four wells in the area are shown in Table 2. Extended leak-off tests (XLOT) provide an improved estimate of the S_{hmin} magnitude: however, no such data are available in the study area. In the absence of XLOT measurements, the lower bound of LOT data provides an estimate of S_{hmin}, although it is noted that XLOTs should be acquired where detailed stress data are required (Addis *et al.* 1998; White *et al.* 2002).

A single LOT value is reported for the 13/24b–3 well, recorded in the Tor Formation in the uppermost part of the Chalk Group. The value reported is close to the calculated S_v of approximately 23.14 MPa at that depth. As the test was taken in strata described as firm–hard limestone at relatively shallow depth (998 m below sea level, as shown in Fig. 8), it is uncertain how the least principal

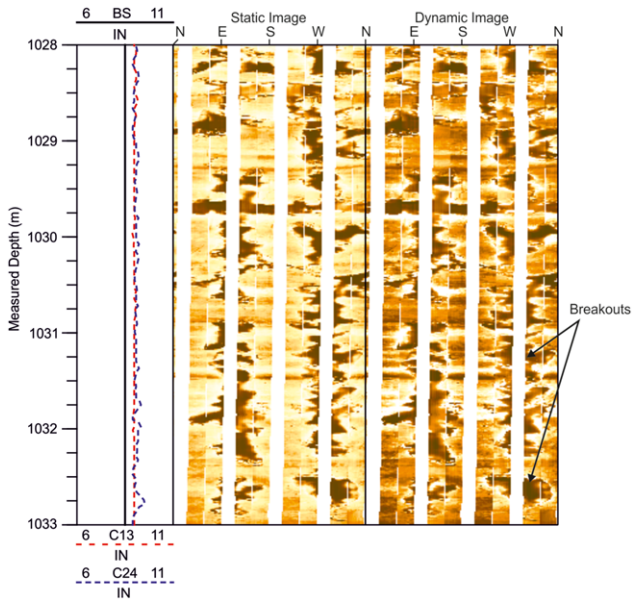

Fig. 5. Example of breakouts from FMI logs in well 13/26a-4. Breakouts are identified by darker conductive zones seen on opposite sides of the borehole wall.

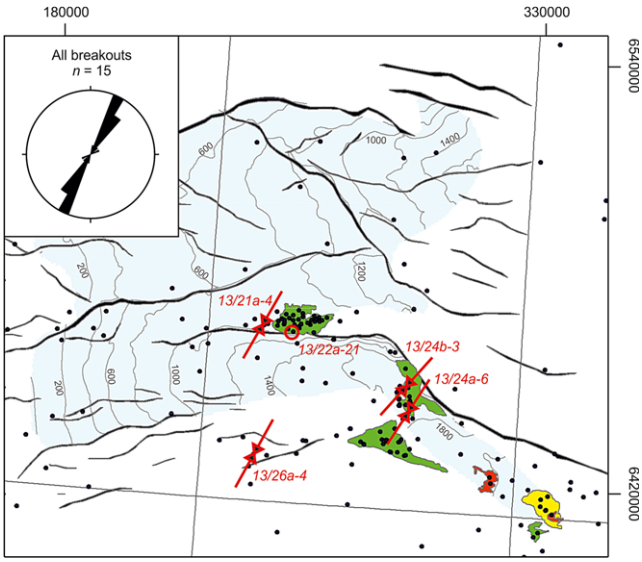

Fig. 6. S_{Hmax} orientations calculated from the observation of borehole breakouts in the study wells across the study region. No stress orientation could be determined for well 13/22a-21.

stress magnitude relates to the unconsolidated sandstones of the Captain Sandstone Member or to the mudstones of the overlying Rodby Formation caprock. The other three reported LOT values were all taken from the Aptian–Barremian-aged Valhall or Wick Sandstone formations, and the values are therefore more likely to represent those applicable to the Captain Sandstone and its clay-rich overburden. A S_{hmin} gradient of 18 MPa km^{-1} relative to the seabed appears to represent a suitable lower bound to the LOT data, and is taken here to represent S_{hmin} in the fault-stability analysis (Fig. 8), although the Tor Formation measurement indicates that the magnitude of S_{hmin} is not a simple linear gradient through the overburden. This gradient is similar to the assumed 18.09 MPa km^{-1} fracture pressure gradient noted by Jin *et al.* (2012). Because leak-off pressure does not provide a direct measurement of S_{hmin}, depending as it does on other factors such as lithology, drilling fluids and wellbore stability, there is inherent uncertainty in the S_{hmin} gradient determined, particularly given the limited number of test data available. The sand-rich nature of the lithologies tested by the lowermost LOT measurements are expected to possess lower fracture pressures than the overburden lithologies, to some extent justifying the use of the lower bound to the LOT data to represent the lower bound of S_{hmin} in the absence of more reliable XLOT data. Using the lower bound as an estimate of S_{hmin} provides larger differential stresses, ensuring that the fault-stability analysis is conservative. Greater differential stresses would result in faults being closer to failure in the current stress regime, while smaller differential stresses will tend to increase the mechanical stability of faults.

According to critically stressed faulting theory, it is possible to determine the upper and lower bound magnitudes of S_{hmin} and S_{Hmax} for any particular depth given knowledge of the pore pressure, S_v and the coefficient of friction. A stress polygon (Moos & Zoback 1990; Zoback *et al.* 2003) can be constructed to illustrate the allowable stress states constrained by the strength of faults optimally orientated for failure in the current stress regime using equation (2), after Jaeger *et al.* (2007):

$$\frac{\sigma_1}{\sigma_3} = \frac{S1 - P_P}{S3 - P_P} \leq [(\mu^2 + 1)^{1/2} + \mu]^2 \quad (2)$$

where P_p is pore pressure, S1 and S3 are respectively the maximum and minimum principal stresses, and μ is the coefficient of friction. Byerlee (1978) shows that, commonly, $0.6 \leq \mu \leq 1$, so a value of 0.6 is taken here as a reasonable assumption for μ, given that the Captain Sandstone is poorly cemented and consolidated. The occurrence or non-occurrence of wellbore breakouts and drilling-induced tensile fractures may be used to estimate the magnitude of S_{Hmax} using equation (3) for drilling-induced tensile fractures and equation (4) for borehole breakouts (see Barton & Zoback 1988; Moos & Zoback 1990; Zoback *et al.* 2003 for derivation of the equations):

$$S_{Hmax} = 3S_{hmin} - 2P_P - \Delta P - T_0 - \sigma^{\Delta T} \quad (3)$$

where ΔP is the difference in pressure between the pore-fluid pressure and the pressure exerted by the column of mud in the wellbore, T_0 is the tensile strength of the rock, and $\sigma^{\Delta T}$ is the stress induced by the temperature differential between the formation and drilling fluids: and for breakouts:

$$S_{Hmax} = \frac{(C_0 + 2P_P + \Delta P + \sigma^{\Delta T}) - S_{hmin}(1 + 2\cos 2\theta_b)}{1 - 2\cos 2\theta_b} \quad (4)$$

where $2\theta_b \equiv \pi - w_{bo}$.

In equation (4), C_0 is the rock strength and W_{bo} represents the width of the observed breakout in units of degrees. Equations (3) and (4) have been used to estimate the magnitude of S_{Hmax} in wells 13/21a–4, 13/24b–3 and 13/26a–4. Figure 9a shows the constraints on the magnitudes of the horizontal stresses at a depth of 1564 m TVDSS (True Vertical Depth Subsea) where breakouts are observed in well 13/24b-3. The lack of tensile fractures over the logged interval suggests that, for a given value of S_{hmin}, the magnitude of S_{Hmax} should fall below the appropriate tensile failure contour denoted by the black dotted line in Figure 9a. The tensile strength of the Captain Sandstone is generally less than 70 kPa (Skopec 2001) and, as such, is considered here to be essentially zero. As shown by Figure 9a, greater tensile strength would reduce the magnitude of S_{Hmax} required to form a drilling-induced tensile fracture for any given value of S_{hmin}. As no information is available regarding the temperature-induced stress perturbation at the depth of interest, this parameter is also assumed to be zero. As shown by Zoback *et al.* (2003), the result of moderate cooling has a limited impact on the tensile fracture contours, whereas modest increases in mud weight

Table 2. *Formation leak-off test data from wells in the study area. The leak-off pressure can be taken as the fracture pressure for the rocks at the depths tested. The lithological descriptions are taken from the company logs*

Well	Depth subsea (m)	Pressure (MPa)	Description
13/24b–3	988	23	Tor Formation – firm to hard limestone
13/22b–4	1563	29	Valhall Formation, Aptian 'Sandy' Unit – soft to firm claystone grading to siltstone in parts
13/22b–19	1611	31	Valhall Formation, Early Aptian – loose sand and soft to firm claystone
13/22b–20	1584	30	Early Barremian Wick Sandstone Formation – loose fine- to medium- grained sandstone and calcareous claystone

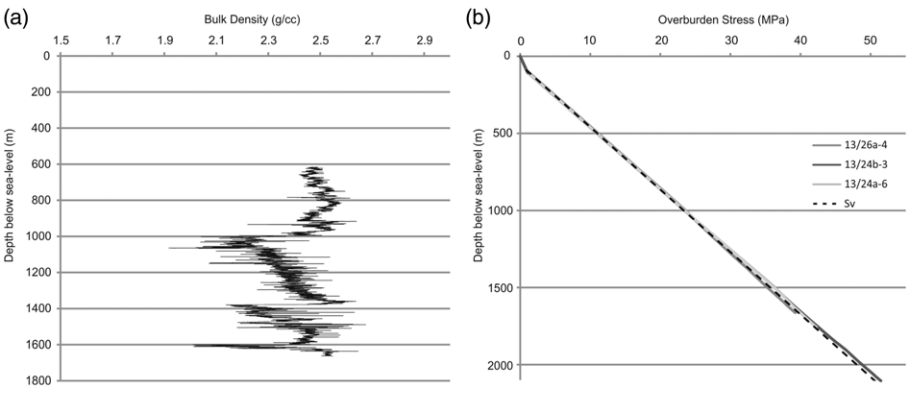

Fig. 7. (**a**) Example of a bulk density log from well 13/26a-4. (**b**) Vertical stress profiles calculated from integration of density logs and the average gradient of S_v used in this study.

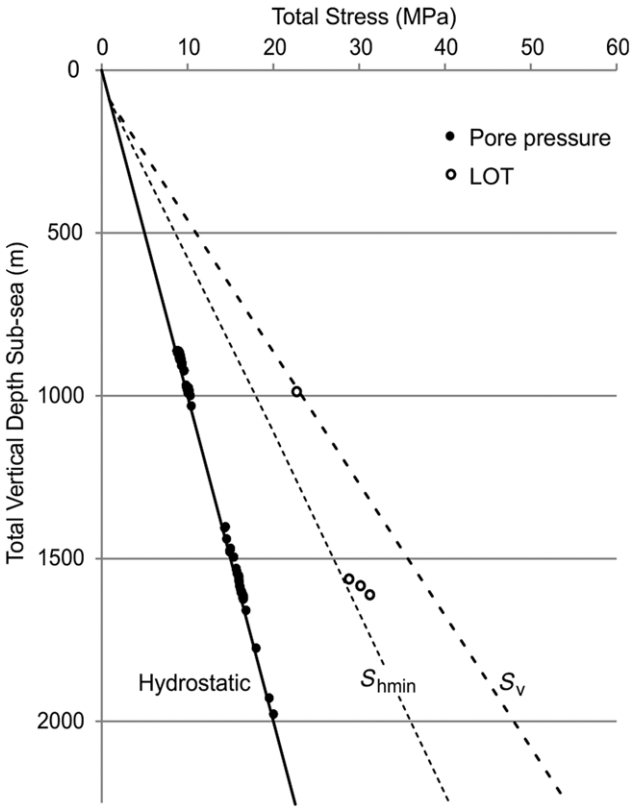

Fig. 8. S_{hmin} stress profile plotted alongside leak-off pressure data, and hydrostatic and lithostatic (S_v) gradients. The S_{hmin} profile is estimated as a lower bound to the leak-off pressure points. As highlighted by the shallowest measurement, standard LOT data are not direct measurements of the least principal stress and so the gradient shown represents an estimate of the lower-bound S_{hmin}.

are far more influential to the formation of drilling-induced tensile fracture. In the event that significant borehole cooling had occurred, the magnitude of S_{Hmax} required to cause the formation of drilling-induced tensile fractures would be reduced for any given magnitude of S_{hmin}, and so the assumption of zero $\sigma^{\Delta T}$ gives an upper bound to the tensile fracture contour, providing the upper possible frictional limit of S_{Hmax}. In the absence of equivalent circulating density data, static mud weight is used to calculate ΔP. Despite the observation of borehole breakouts, the borehole breakout contours cannot be used

Table 3. *Constraints on principal stress magnitudes used in the fault-stability study*

	Stress magnitude gradients (MPa km^{-1} relative to seabed)		
	Strike-slip	Normal/strike-slip	Normal
S_v	25	25	25
S_{Hmax}	31.95	25	18
S_{hmin}	18	18	18

to accurately constrain the magnitude of S_{Hmax} as a function of S_{hmin} because the strength of the rock is unknown. However, contours are plotted for different rock strength values using equation (4) and the average breakout width in well 13/24b-3 of 41.6° (Fig. 9a). These contours may be used to provide constraints on the strength of the rock given the end-member magnitude of S_{Hmax} allowable. As breakouts have been observed, the magnitude of S_{Hmax} should lie above the appropriate rock strength contour. Breakout width can be difficult to measure accurately from image logs, and so this is considered an uncertain parameter and the breakout contours are not used here to predict the magnitude of S_{Hmax}. Figure 9b shows the maximum allowable values of S_{Hmax} obtained from the analyses described above for each depth where borehole breakout has been observed. Albeit highly uncertain due to the uncertainty of the input parameters, a linear S_{Hmax} gradient of 31.95 MPa to the seabed has been derived from the outer envelope of the measurements in the three wells. This provides the end-member conservative case for the fault-stability study where differential stresses are at a maximum. As $S_{Hmax} > S_v > S_{hmin}$, this would imply a strike-slip faulting stress state after Anderson (1951). As the true magnitude of S_{Hmax} is unknown and might, in fact, be significantly lower, a further two stress magnitude cases are considered for the fault-stability study corresponding to the normal/strike-slip and normal faulting stress states (Table 3).

Fault-stability analysis

The stress orientations derived from borehole breakouts, and the stress magnitude gradients shown in Table 3, have been used to resolve the shear and normal stresses onto the faults using the 3D geological model. As the magnitude of S_{Hmax} is uncertain, all three cases have been considered. Slip tendency (T_s), the ratio of shear to normal stress (Morris *et al.* 1996; Ferrill *et al.* 1999), has subsequently been calculated for each node on the fault planes

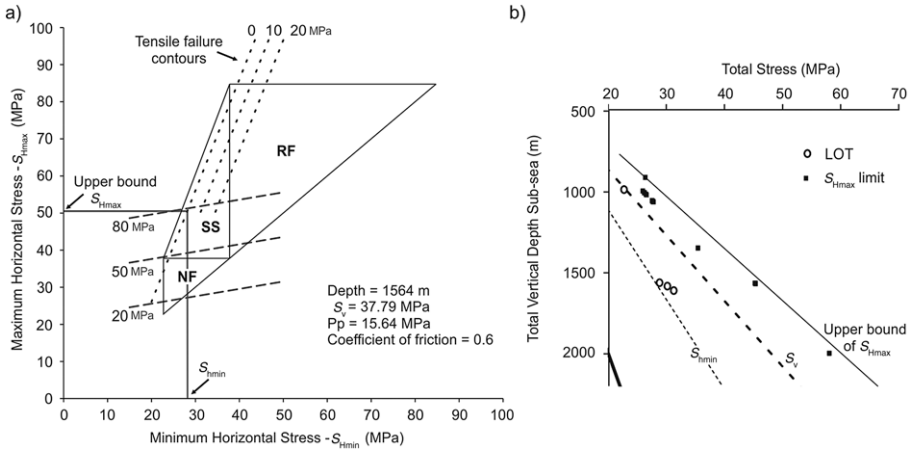

Fig. 9. (**a**) Polygon used to constrain the horizontal stress magnitudes at a depth of 1564 m below sea level in well 13/24b-3. The outer polygon limits the stress magnitudes by the strength of optimally orientated faults, and is divided into normal (NF), strike-slip (SS) and reverse faulting (RF) stress states. The tensile failure contours are shown by the dotted lines, while breakout contours are shown by dashed lines for various compressive rock strengths. The value of S_{hmin} determined from the LOT data and the corresponding maximum possible value of S_{Hmax} are also shown. (**b**) Maximum allowable S_{Hmax} magnitude for each depth where borehole breakouts have been observed, alongside stress gradients, with the upper bound of S_{Hmax} constrained by the absence of drilling-induced tensile fractures.

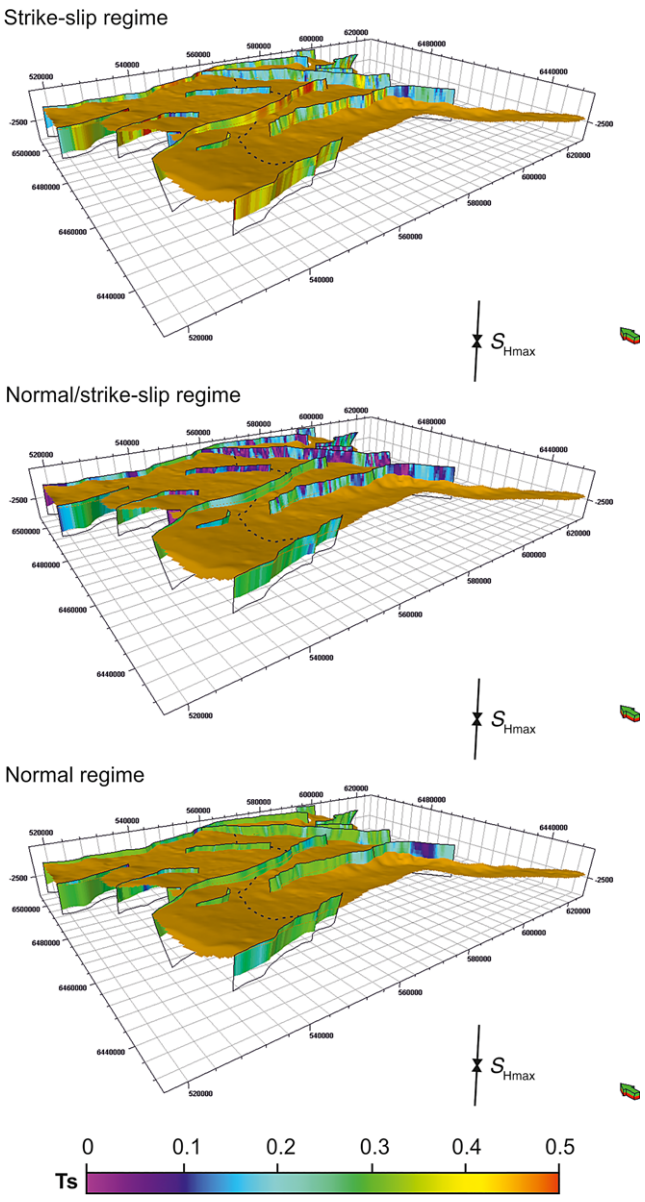

Fig. 10. Comparison of slip-tendency values on mapped faults in the study area, for different stress states as detailed in Table 3. Note that the slip tendency is scaled to 0.5 to highlight those faults with higher values closer to μ. The top Captain Sandstone surface is shown for reference. The 800 m depth contour is shown as a black dotted line.

(Fig. 10). A slip tendency value equal to the coefficient of friction (μ) corresponds to the frictional strength of a cohesionless fault: so faults or, more accurately, fault segments that have T_s values close to 0.6 are most susceptible to reactivation in this analysis. The slip tendency of a fault depends on both the dip and the strike of the fault in relation to the stress tensor. A number of cases worldwide highlight that critically stressed faults are more likely to be hydraulically conductive than non-critically stressed faults (Barton *et al.* 1995; Wiprut & Zoback 2000; Finkbeiner *et al.* 2001; Hennings *et al.* 2012). Despite this, it must be noted that this is a conservative approach, as reactivated faults will not necessarily become fluid-flow pathways (Bjørlykke *et al.* 2005) and in addition, fault zones are not always characterized by cohesionless interfaces, so the assumption that the faults have zero cohesion is also conservative.

The slip tendency calculated for the strike-slip case is highly variable, with higher shear stresses acting on faults orientated close to approximately 30° from S_{Hmax}, resulting in some faults being susceptible to reactivation. Faults orientated perpendicular to the direction of S_{Hmax} exhibit lower slip tendencies as a result of higher normal stresses. The normal/strike-slip case exhibits much lower slip tendencies, with no fault segments possessing a slip tendency greater than 0.3. Faults striking sub-parallel to S_{Hmax} again possess the higher values of slip tendency. The normal faulting case possesses the least variation in slip tendency, with values of approximately 0.3 over most of the fault nodes, with the clear exception of the eastern part of the South Halibut Fault, which dips at a steeper angle of about 80° and is therefore less susceptible to failure in a normal faulting stress state. In this case, despite many of the faults dipping at optimal angles close to 60° (30° from S_v), none of the fault segments have particularly high slip tendencies because the gradient of S_{hmin} implies values higher than the frictional minimum illustrated by the stress polygon in Figure 9a. It is worth noting that, although the faults shown by Figure 10 extend from the Captain Sandstone and through the overburden to the seabed, the majority of the pressure increase resulting from the injection of CO_2 will be confined to the reservoir interval into which CO_2 is injected. Segments of faults with high slip tendencies in the shallower section are therefore less likely to experience a significant increase in pore-fluid pressure unless the fault zones become a conduit for fluid flow (either CO_2 or displaced formation fluids) from greater depths.

The slip-tendency results presented are dependent on the reliability of the 3D fault model and the validity of the input stress field (Worum *et al.* 2004). As the fault model presented is based on regional mapping using 2D seismic reflection profiles, with regional depth conversion applied, the model will inevitably contain some geometrical inaccuracies that will affect the calculated values. In particular, the depth conversion can affect the dip of the faults, which is critical as it affects the angle of the fault plane relative to the stress tensor. Despite this, the main structural trends are captured by the geological model, and the results are useful in assessing fault risk at the basin scale.

The susceptibility to failure of faults at a given depth can also be expressed in terms of the pore-pressure perturbation required in order to cause the reactivation of faults, known as the fracture stability. Fracture stability for the stress regimes shown in Table 3 are illustrated by Figure 11 for a depth of 1200 m. This is the average depth of the Captain Sandstone below 800 m, where it is most prospective for CO_2 storage and injected CO_2 would be expected to remain in its dense phase (Chadwick *et al.* 2008). Because not all faults and fractures will be accurately mapped using seismic reflection data, stereographic projections are useful as they can be used to calculate the change in pore pressure required to reactivate faults of any orientation at a given depth.

Poroelastic effects on fault stability are illustrated in Figure 12. Owing to coupling between pore pressure and stress (Hillis 2000), horizontal stress magnitudes are likely to decrease during depletion (Streit & Hillis 2004), and to increase during injection. Equation (5), after Brown *et al.* (1994), can be used to estimate the poroelastic effect in reservoirs with a high lateral extent compared to thickness:

$$\Delta S_{Hor} = \alpha \frac{(1-2\nu)}{(1-\nu)} \Delta P_P \quad (5)$$

where S_{Hor} is both S_{Hmax} and S_{hmin}, α is Biot's coefficient and ν is Poisson's ratio. For reasonable values for α=1 and ν=0.25 (Chiaramonte *et al.* 2008; McDermott *et al.* 2016), the horizontal stresses will increase by 2 MPa as a result of a 3 MPa pore-pressure increase, a reasonable far-field pore-pressure perturbation (Jin *et al.* 2012). It is noted that equation (5) should not be used for predicting actual stress values at depth as it has been derived for a homogeneous, isotropic and linear poroelastic reservoir. Nevertheless, it provides a useful guide as to the likely poroelastic effects that might result from CO_2 injection and the subsequent

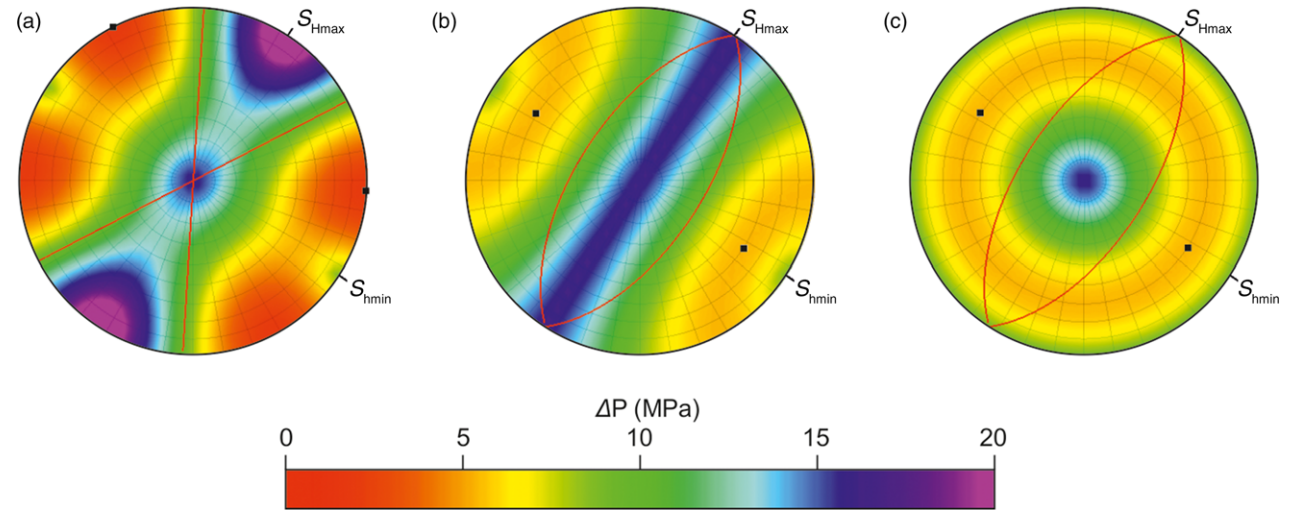

Fig. 11. Fault stability represented as equal-angle, lower-hemisphere stereographic poles to planes for (**a**) strike-slip, (**b**) normal/strike-slip and (**c**) normal faulting stress states at a depth of 1200 m below sea level. The numerical values refer to the increase in fluid pressure (ΔP) required to cause fault reactivation, assuming a Griffith–Coulomb failure envelope for cohesionless faults with a value of μ of 0.6.

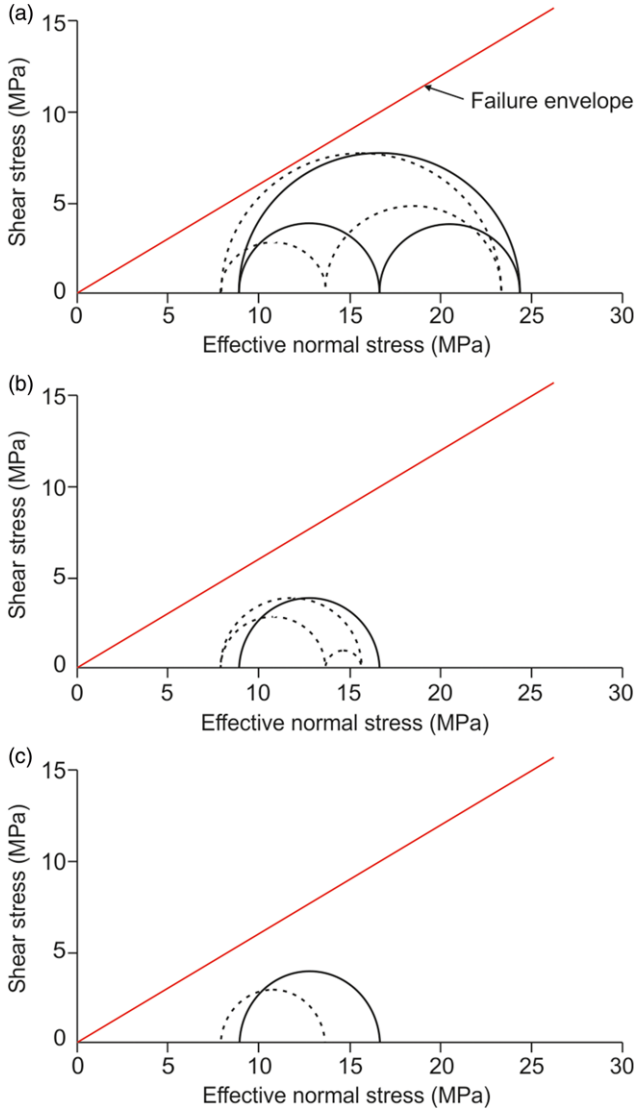

Fig. 12. Mohr–Coulomb diagrams showing stress states in relation to a cohesionless fault-failure envelope at a depth of 1200 m below sea level for (**a**) strike-slip, (**b**) normal/strike-slip and (**c**) normal faulting stress states. Poro-elastic stress change is shown for a pressure increase of 3 MPa. The pre-injection cases are shown as solid circles and the post-injection cases shown as dotted circles.

pressure increases. This effect would be largely constrained to the reservoir interval where the majority of the pressure perturbation will occur during injection.

The results shown in Figures 11 and 12 show that the change in pore pressure (ΔP) required to cause fault reactivation varies considerably across the different stress states. In the strike-slip stress state, optimally orientated faults at virgin reservoir pressures are approximately 1.5 MPa from failure, moving to approximately 0.5 MPa after a perturbation of 3 MPa (Fig. 12a). The poroelastic effect counteracts the effect of the reducing effective stresses, increasing the stability of the faults somewhat and allowing the faults to sustain more pressure than if the poroelastic effect is discounted. Chiaramonte *et al.* (2008) similarly found that the poroelastic effect increased the pressure required to cause failure of a fault bounding a prospective CO_2 storage site in the USA. In the normal/strike-slip stress state, optimally orientated faults that strike parallel to S_{Hmax} and dip at angles of 60° will fail at increased fluid pressures of approximately 5 MPa. Once poroelastic effects are accounted for, the stress state transitions to a strike-slip faulting regime as S_{Hmax} exceeds the magnitude of S_v (Fig. 12b). Optimally orientated faults are then vertical faults striking at angles of 30° from S_{Hmax}, and will fail at slightly lower pressures. In the normal stress state, where $S_{Hmax} = S_{hmin}$, faults dipping at 30° and striking in any orientation are those that are most susceptible to failure, with a required pore-pressure increase of approximately 5 MPa. Little change in the fault stability is seen once the poroelastic effect is considered, as the difference between the horizontal stress and S_v magnitude is reduced, resulting in a smaller Mohr circle (Fig. 12c). For comparison, a simplified analysis from the southern part of the North Sea suggests that a lower-bound pore-pressure increase of 3.3 MPa could be obtained without reactivating existing faults at a depth of 1000 m based on a simple, yet conservative, geomechanical analysis (Williams *et al.* 2014).

Thermal stress resulting from injection of cold or warm fluid into a rock mass can also affect fault stability in the near-well region, and can result in stress conditions moving closer towards failure. The effect of the thermal-stress perturbation due to CO_2 injection into the Captain Sandstone has been presented elsewhere using a coupled numerical thermal and mechanical modelling tool (McDermott *et al.* 2016). The study found that the change in the stress field resulting from the combination of pore-pressure and thermal-stress effects is dependent on the permeability structure of different layers, such as the reservoir, underburden, primary caprock and overburden. Stress

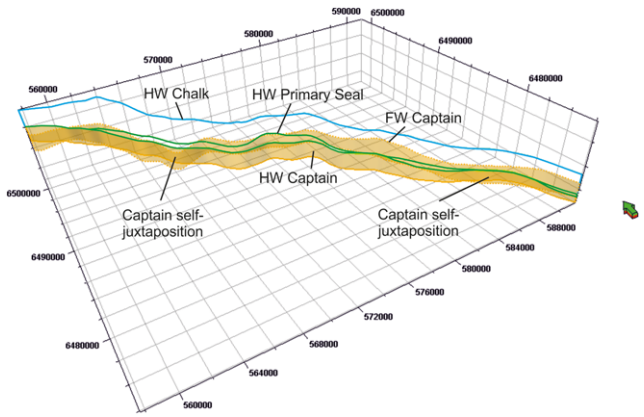

Fig. 13. Fault-juxtaposition Allan diagram showing the self-juxtaposition of the Captain Sandstone (darker shade) and the hanging-wall extent of the Rodby and Carrack formation primary seal and the Chalk Group secondary seal. HW, hanging wall; FW, footwall.

bridging and redistribution between layers with different mechanical properties can, in some cases, lead to enhanced geomechanical stability in the caprock (McDermott *et al.* 2016).

The presented fault-stability analysis considers only the effect of increasing the pore-fluid pressures as a result of CO_2 injection. Production-induced stress perturbations have not been considered here, but are noteworthy given the history of hydrocarbon production from the Captain Sandstone reservoir in the Moray Firth and the current interest in storage of CO_2 in depleted fields. Such effects should be studied on a site-specific scale, where knowledge of the full production history (including water injection, if applicable) is available. Such an in-depth study has been conducted for the proposed storage project at the Goldeneye Field (Shell 2011*b*), which found that geomechanical effects are not prohibitive to the proposed storage plans.

Discussion

Both migration and pressure limitations act to constrain the volumes of CO_2 that can be stored in subsurface reservoirs (Williams *et al.* 2013). In relation to the geomechanical stability of faults, it is therefore important to consider both the pressure propagation and the expected distribution of the CO_2 during the injection period and subsequently until the plume has stabilized. It is feasible that a far-field fault might be reactivated during CO_2 injection, but that the CO_2 would be confined to some area remote from the reactivated fault segment. In such a case, the reactivated fault would not compromise storage integrity. It would be possible, therefore, to optimize CO_2 storage activities by avoiding injection into areas from which CO_2 would be likely to migrate towards critically stressed faults, as identified by Figure 10. Jin *et al.* (2012) considered simulations of CO_2 injection into the Captain Sandstone in which faults were considered to be non-transmissible to fluid flow and where hydraulic communication was permitted across them. Potential migration pathways between fault blocks can be identified using fault-plane Allan diagrams (Allan 1989), where stratigraphic intersections with the fault are mapped onto the fault plane. In the case of the Little Halibut Fault, a significant potentially compartmentalizing fault (Fig. 1), the Captain Sandstone in the footwall block is not juxtaposed against permeable formations above the primary and secondary top seals (Fig. 13). Considering the aquifer conservatively as a closed system, the storage capacities calculated by Jin *et al.* (2012) are 362 and 358 Mt, respectively, for cases where faults are open or closed to flow, a reduction of less than 1%. Other factors controlling the cumulative injected CO_2 in the simulations are therefore more significant than flow or flow retardation across the faults. In terms of the major faults included in the model, cross-fault migration is expected to be fairly insignificant due to juxtaposition of the reservoir footwall blocks against primary or secondary sealing formations (Fig. 13), and along- or up-fault migration constitutes the greater risk to containment of any injected CO_2. Careful juxtaposition mapping, preferably using 3D seismic reflection data, should be carried out in the vicinity of proposed CO_2 injection sites.

In the fault-stability analysis presented, relatively few observed fault segments are seen to be critically stressed and so, provided that far-field pressure can be sustained at a reasonable level and CO_2 isolated from near-critically stressed fault segments, the risk of leakage via faults can be seen as fairly low. It is possible that smaller faults not observed might be more optimally orientated for reactivation: however, it is argued that these are likely to be less extensive in terms of throw and vertical extent (as they are not observed on seismic reflection data), and as such will not necessarily penetrate the entire reservoir top seal and provide a conduit for injected CO_2 if reactivation was to occur.

Although the analysis presented assumes that critically stressed faults in the current stress regime will present a risk to storage integrity due to an increase in along-fault permeability during slip, it has been shown that shear-stress hysteresis during uplift and exhumation can also affect the ability of faults to conduct fluids, even if they are not critically stressed in the present stress state (Sathar *et al.* 2012). Experiments on synthetic fault gouge composed of pure kaolinite found that, although fault orientation does have an effect on gas entry pressure, non-optimally orientated faults can also experience flow (Cuss *et al.* 2015). In addition, reactivation of a fault will not necessarily increase the permeability of the fault plane because in some materials, such as weakly cemented sand, initial dilation and continued shearing will result in the formation of low-porosity/low-permeability material (Bjørlykke *et al.* 2005). Processes such as clay smear can also act to reduce fault-zone permeability, and so the assumption that a reactivated fault will permit vertical flow of CO_2 is conservative.

Conclusions

The *in situ* stress field affecting the Captain Sandstone in the Inner Moray Firth area, a potential target for CO_2 storage, has been evaluated. The available data suggest that either normal, strike-slip or normal/strike-slip transitional faulting stress regimes might prevail at reservoir depth in the region, while the observation of borehole breakouts indicate a relatively uniform direction of S_{Hmax}, orientated NNE–SSW. The magnitudes of the principal stresses have been determined for each of the possible stress regimes using integrated density logs, LOTs, borehole image logs and frictional faulting limits. Where stress-magnitude parameters are regarded to be uncertain, the analysis has assumed large differential stresses, meaning that a conservative approach has been taken to the fault-stability analysis. Given the paucity and quality of available stress-field indicators and measurements, such an approach is useful in determining the low end-member constraints on the pore-pressure window with which to operate without reactivating existing faults.

The stress tensor has been resolved onto 3D fault planes, derived from an existing geological model of the Captain Sandstone and its overburden, to evaluate the susceptibility of the larger faults to reactivation, the risk of which might be increased if pore-fluid pressure increases as a result of large-scale CO_2 injection. The results suggest that some segments of the regional faults are likely to be near-critically stressed under some of the possible stress conditions, and therefore would not require a considerable pore-pressure increase in order to become reactivated. It is likely, however, that smaller local faults will become reactivated first. If this occurs in the area outside of the CO_2 plume footprint, formation

brine rather than CO_2 would leak-off from the reservoir, potentially relieving some reservoir pressure (Hannis *et al.* 2013). As slip on existing faults could facilitate a risk to CO_2 storage integrity, it is suggested that aspects surrounding the *in situ* stress conditions (both regional and local) are critically assessed during site appraisal. In addition, thermal stresses, which affect an area relatively local to the injection well, have not been considered here, but can significantly alter the stress state locally as a result of the injection of cold fluid, and should be examined by coupled flow–geomechanical models (McDermott *et al.* 2016).

The results presented provide a useful indication of the fault geometries most susceptible to reactivation in the current *in situ* stress conditions across the IMF, at depths where CO_2 might be injected. To account for uncertainty in principal stress magnitudes, high differential stresses have been assumed in the analysis, providing conservative estimates of fault stability. Detailed geological models and data pertaining to pore pressure, rock mechanics and stress will be required to more accurately investigate fault stability for specific storage sites.

Acknowledgements and Funding

Badley Geoscience Ltd are thanked for the use of their TrapTester software, which was used to generate the stereographic projections. The authors would also like to acknowledge the financial support of the UK CCS Research Centre (www.ukccsrc.ac.uk) in carrying out this work. The UKCCSRC is funded by the EPSRC as part of the RCUK Energy Programme. This paper is published with the permission of the Executive Director, British Geological Survey (NERC).

References

Aadnoy, B.S. & Bell, J.S. 1998. Classification of drill-induced fractures and their relationship to in-situ stress directions. *Log Analyst*, **39**, 27–42.

Addis, M.A., Hanssen, T.H., Yassir, N., Willoughby, D.R. & Enever, J. 1998. *A comparison Of Leak-Off Test And Extended Leak-Off Test Data For Stress Estimation*. SPE/ISRM 47235, 131–140.

Ahmadi, Z.M., Sawyers, M., Kenyon-Roberts, S., Stanworth, C.W., Kugler, K. A., Kristensen, J. & Fugelli, E.M.G. 2003. Paleocene. *In:* Evans, D., Graham, C., Armour, A. & Bathurst, P. (eds) *The Millennium Atlas: Petroleum Geology of the Central and Northern North Sea*. Geological Society, London, 235–259.

Akhurst, M., Hannis, S.D. *et al.* 2015. Risk Assessment-Led Characterisation of the SiteChar UK North Sea Site for the Geological Storage of CO_2. *Oil & Gas Science and Technology – Revue d'IFP Energies nouvelles*, **70**, 567–586.

Allan, U.S. 1989. Model for hydrocarbon migration and entrapment within faulted structures. *American Association of Petroleum Geologists Bulletin*, **73**, 803–811.

Anderson, E.M. 1951. *The Dynamics of Faulting and Dyke Formation with Applications to Britain*. Oliver & Boyd, Edinburgh.

Argent *et al.* 2002. Heterogeneous exhumation in the Inner Moray Firth, UK North Sea: constraints from new AFTA® and seismic data. *Journal of the Geological Society, London*, **159**, 715–729, http://doi.org/10.1144/0016-764901-141

Aydin, A. 2000. Fractures, faults, and hydrocarbon entrapment, migration and flow. *Marine and Petroleum Geology*, **17**, 797–814.

Barton, C.A. & Zoback, M.D. 1988. In-situ stress orientation and magnitude at the Fenton Geothermal Site, New Mexico, determined from wellbore breakouts. *Geophysical Research Letters*, **15**, 467–470.

Barton, C.A., Zoback, M.D. & Moos, D. 1995. Fluid flow along potentially active faults in crystalline rock. *Geology*, **23**, 683–686.

Bell 1990. Investigating stress regimes in sedimentary basins using information from oil industry wireline logs and drilling records. *In:* Hurst, A., Lovell, M.A. & Morton, A.C. (eds) *Geological Applications of Wireline Logs*. Geological Society, London, Special Publications, **48**, 305–325, http://doi.org/10.1144/GSL.SP.1990.048.01.26

Bjørlykke, K., Høeg, K., Faleide, J.I. & Jahren, J. 2005. When do faults in sedimentary basins leak? Stress and deformation in sedimentary basins; examples from the North Sea and Haltenbanken, offshore Norway. *American Association of Petroleum Geologists Bulletin*, **89**, 1019–1031.

Brown, K.M., Bekins, B., Clennell, B., Dewhurst, D. & Westbrook, G.K. 1994. Heterogeneous hydrofracture development and accretionary fault dynamics. *Geology*, **22**, 259–262.

Byerlee, J.D. 1978. Friction of rock. *Pure and Applied Geophysics*, **116**, 615–626.

Caine, J.S., Evans, J.P. & Forster, C.B. 1996. Fault zone architecture and permeability structure. *Geology*, **24**, 1025–1028.

Chadwick, R.A., Arts, R., Bernstone, C., May, F., Thibeau, S. & Zweigel, P. 2008. *Best Practise for the Storage of CO_2 in Saline Aquifers*. British Geological Survey, Keyworth, Occasional Publications, **14**.

Chadwick *et al.* 2009*a*. Review of monitoring issues and technologies associated with the long-term underground storage of carbon dioxide. *In:* Evans, D. & Chadwick, R.A. (eds) *Underground Gas Storage: Worldwide Experiences and Future Development in the UK and Europe*. Geological Society of London, London, Special Publications, **313**, 257–275, http://doi.org/10.1144/SP313.15

Chadwick *et al.* 2009*b*. Flow processes and pressure evolution in aquifers during the injection of supercritical CO_2 as a greenhouse gas mitigation measure. *Petroleum Geoscience*, **15**, 59–73, http://doi.org/10.1144/1354-079309-793

Chiaramonte, L., Zoback, M.D., Friedmann, J. & Stamp, V. 2008. Seal integrity and feasibility of CO_2 sequestration in the Teapot Dome EOR pilot: geomechanical characterization. *Environmental Geology*, **54**, 1667–1675.

Copestake, P., Sims, A.P., Crittenden, S., Hamar, G.P., Ineson, J.R., Rose, P.T. & Tringham, M.E. 2003. Lower Cretaceous. *In:* Evans, D., Graham, C., Armour, A. & Bathurst, P. (eds) *The Millennium Atlas: Petroleum Geology of the Central and Northern North Sea*. Geological Society, London, 191–211,

Cowgill, S.M., Meredith, P.G., Murrell, S.A.F. & Brereton, N.R. 1993. Crustal stresses in the North Sea from breakouts and other borehole data. *International Journal of Rock Mechanics and Mining Sciences & Geomechanics Abstracts*, **30**, 1111–1114.

Cuss, R.J., Harrington, J.F., Noy, D.J., Sathar, S. & Norris, S. 2015. An experimental study of the flow of gas along synthetic faults of varying orientation to the stress field: Implications for performance assessment of radioactive waste disposal. *Journal of Geophysical Research: Solid Earth*, **120**, 3932–3945.

Du, K.E., Pai, S., Brown, J., Moore, R.M. & Simmons, M. 2000. Optimising the development of Blake Field under tough economic and environmental conditions. Paper SPE 64714 presented at the International Oil and Gas Conference and Exhibition in China, Beijing, China, 7–10 November 2000.

Faulkner, D.R., Jackson, C.A.L., Lunn, R.J., Schlische, R.W., Shipton, Z.K., Wibberley, C.A.J. & Withjack, M.O. 2010. A review of recent developments concerning the structure, mechanics and fluid flow properties of fault zones. *Journal of Structural Geology*, **32**, 1557–1575.

Ferrill, D.A., Winterle, J., Wittmeyer, G., Sims, D., Colton, S. & Armstrong, A. 1999. Stressed Rock Strains Groundwater at Yucca Mountain, Nevada. *GSA Today*, **9**, 1–8.

Finkbeiner, T., Zoback, M., Flemings, P. & Stump, B. 2001. Stress, pore pressure, and dynamically constrained hydrocarbon columns in the South Eugene Island 330 Field, northern Gulf of Mexico. *American Association of Petroleum Geologists Bulletin*, **85**, 1007–1031.

Garrett *et al.* 2000. Lower Cretaceous deep-water sandstone reservoirs of the UK Central North Sea. *Petroleum Geoscience*, **6**, 231–240, http://doi.org/10.1144/petgeo.6.3.231

Gölke, M. & Coblentz, D. 1996. Origins of the European regional stress field. *Tectonophysics*, **266**, 11–24.

Hannis, S.D., Bricker, S., Goater, A., Holloway, S., Rushton, J., Williams, G. & Williams, J. 2013. Cross-international boundary effects of CO_2 injection. *Energy Procedia*, **37**, 4927–4936.

Heidbach, O., Tingay, M., Barth, A., Reinecker, J., Kurfeß, D. & Müller, B. 2010. Global crustal stress pattern based on the World Stress Map database release 2008. *Tectonophysics*, **482**, 3–15.

Hennings, P., Allwardt, P. *et al.* 2012. Relationship between fractures, fault zones, stress, and reservoir productivity in the Suban gas field, Sumatra, Indonesia. *American Association of Petroleum Geologists Bulletin*, **96**, 753–772.

Hillis, R.R. 2000. Pore pressure/stress coupling and its implications for seismicity. *Exploration Geophysics*, **31**, 448–454.

Hillis & Nelson, 2005. *In situ* stresses in the North Sea and their implications: petroleum geomechanics from exploration to development. *In:* Dóre, A.G. & Vining, B.A. (eds) *Petroleum Geology: North-West Europe and Global Perspectives – Proceedings of the 6th Petroleum Geology Conference*. Geological Society, London, 551–564, http://doi.org/10.1144/0060551

Hillis, R.R., Thomson, K. & Underhill, J.R. 1994. Quantification of Tertiary erosion in the Inner Moray Firth using sonic velocity data from the Chalk and Kimmeridge Clay. *Marine and Petroleum Geology*, **11**, 283–293.

Hilton, V.C. 1999. *Structural and Sedimentological Interpretation of STAR Image Data, Core Sedimentology and Petrography*. BG Exploration and Production, Blake Field, Well 13/24a-6, Report.

Holloway, S. 2009. Storage capacity and containment issues for carbon dioxide capture and geological storage on the UK continental shelf. *Proceedings of the Institution of Mechanical Engineers. Part A, Journal of Power and Energy*, **223**, 239–248.

IPCC. 2005. *IPCC Special Report on Carbon Dioxide Capture and Storage*. Working Group III of the Intergovernmental Panel on Climate Change (Metz, B., Davidson, O., de Coninck, H.C., Loos, M. & Meyer, L.A., eds). Cambridge University Press, Cambridge.

Jaeger, J.C., Cook, N.G.W. & Zimmerman, R. 2007. *Fundamentals of Rock Mechanics*. Blackwell, Oxford.

Jin, M., Mackay, E., Quinn, M., Hitchen, K. & Akhurst, M. 2012. Evaluation of the CO_2 storage capacity of the Captain Sandstone Formation. Paper SPE 154539 presented at the EAGE/SPE Europec Conference and Exhibition, Copenhagen, Denmark, 4–7 June 2012.

Johnson, H. & Lott, G.K. 1993. Cretaceous of the Central and Northern North Sea. *In:* Knox, R.W.O'B. & Cordey, W.G. (eds) *Lithostratigraphic Nomenclature of the UK North Sea*. British Geological Survey, Nottingham.

Kingdon, A., Fellgett, M.W. & Williams, J.D.O. 2016. Use of borehole imaging to improve understanding of the in-situ stress orientation of Central and Northern England and its implications for unconventional hydrocarbon resources. *Marine and Petroleum Geology*, **73**, 1–20.

Law *et al.* 2000. The Kopervik Fairway, Moray Firth, UK. *Petroleum Geoscience*, **6**, 265–274, http://doi.org/10.1144/petgeo.6.3.265

Mardia, K.V. 1972. *Statistics of Directional Data: Probability and Mathematical Statistics*. Academic Press, San Diego, CA.

Marshall *et al.* 2016. Goldeneye: modelling a depleted field for carbon capture – how much uncertainty is left? *Petroleum Geoscience*, **22**, 37–45, http://doi.org/10.1144/petgeo2014-072

McDermott, C.I., Williams, J., Tucker, O., Jin, M., Mackay, E., Edlmann, K. & Akhurst, M. 2016. Simple effective tool for screening the geomechanical stability (thermal & mechanical) of shared multi-user CO_2 storage assets. *International Journal of Greenhouse Gas Control*, **45**, 43–61.

Moos, D. & Zoback, M.D. 1990. Utilization of observations of well bore failure to constrain the orientation and magnitude of crustal stresses: application to continental, Deep Sea Drilling Project, and Ocean Drilling Program boreholes. *Journal of Geophysical Research*, **95**, 9305–9325.

Morris, A., Ferrill, D.A. & Henderson, D.B. 1996. Slip-tendency analysis and fault reactivation. *Geology*, **24**, 275–278.

Noy, D.J., Holloway, S., Chadwick, R.A., Williams, J.D.O., Hannis, S.D. & Lahann, R.W. 2012. Modelling large-scale carbon dioxide injection into the Bunter Sandstone in the UK Southern North Sea. *International Journal of Greenhouse Gas Control*, **9**, 220–233.

Oakman 2005. The Lower Cretaceous plays of the Central and Northern North Sea: Atlantean drainage models and enhanced hydrocarbon potential. *In:* Doré, A.G. & Vining, B.A. (eds) *Petroleum Geology: North-West Europe and Global Perspectives – Proceedings of the 6th Petroleum Geology Conference*. Geological Society, London, 187–198, http://doi.org/10.1144/0060187

Pinnock & Clitheroe 2003. The Captain Field, Block 13/22a, UK North Sea. *In:* Gluyas, J.G. & Hichens, H.M. (eds) *United Kingdom Oil and Gas Fields, Commemorative Millennium Volume*. Geological Society, London, Memoirs, **20**, 431–441, http://doi.org/10.1144/GSL.MEM.2003.020.01.35

Plumb, R.A. & Hickman, S.H. 1985. Stress-induced borehole enlargement: a comparison between the four-arm dipmeter and the borehole televiewer in the Auburn geothermal well. *Journal of Geophysical Research*, **90**, 5513–5521.

Quinn, M.F., Callaghan, E. & Hitchen, K. 2010. *Scottish CCTS Development Study: The mapping and characterisation of the Captain Sandstone saline aquifer, Moray Firth*. British Geological Survey Report, CR/10/114. British Geological Survey, Nottingham.

Richardson *et al.* 2005. Role of Cenozoic fault reactivation in controlling pre-rift plays, and the recognition of Zechstein Group evaporite–carbonate lateral facies transitions in the East Orkney and Dutch Bank basins, East Shetland Platform, UK North Sea. *In:* Doré, A.G. & Vining, B.A. (eds) *Petroleum Geology: North-West Europe and Global Perspectives – Proceedings of the 6th Petroleum Geology Conference*. Geological Society, London, 337–348, http://doi.org/10.1144/0060337

Rose 1999. Reservoir characterization in the Captain Field: integration of horizontal and vertical well data. *In:* Fleet, A.J. & Boldy, S.A.R. (eds) *Petroleum Geology of Northwest Europe: Proceedings of the 5th Petroleum Geology Conference*. Geological Society, London, 1101–1114, http://doi.org/10.1144/0051101

Rose *et al.* 2000. Sand body geometry, constrained and predicted during a horizontal drilling campaign in a Lower Cretaceous turbidite sand system, Captain Field, UKCS Block 13/22a. *Petroleum Geoscience*, **6**, 255–263, http://doi.org/10.1144/petgeo.6.3.255

Sathar, S., Reeves, H.J., Cuss, R.J. & Harrington, J.F. 2012. The role of stress history on the flow of fluids through fractures. *Mineralogical Magazine*, **76**, 3165–3177.

SCCS. 2011. *Progressing Scotland's CO_2 Storage Opportunities*. Scottish Centre for Carbon Storage, Edinburgh, http://www.sccs.org.uk/images/expertise/reports/progressing-scotlands-co2/ProgressingScotlandCO2Opps.pdf [last accessed: January 2016].

Shell. 2011*a*. *Static Model Field Report*. ScottishPower CCS Consortium, UK Carbon Capture and Storage Demonstration Competition Report, UKCCS–KT-S7.21-Shell–002.

Shell. 2011*b*. *Geomechanics Summary Report*. ScottishPower CCS Consortium, UK Carbon Capture and Storage Demonstration Competition Report, UKCCS–KT-S7.19-Shell–004.

Skopec, R.A. 2001. *Geomechanical Evaluation of the Lower Captain Sandstone, UKCS – Compaction and Sand Control Issues in a Poorly Consolidated Heavy Oil Reservoir*. Executive Summary Report. Petrophysical Applications International Inc., Spring, TX.

Sperner *et al.* 2003. Tectonic stress in the Earth's crust: advances in the World Stress Map project. *In:* Nieuwland, D. (ed.) *New Insights into Structural Interpretation and Modelling*. Geological Society, London, Special Publications, **212**, 101–116, http://doi.org/10.1144/GSL.SP.2003.212.01.07

Streit, J.E. & Hillis, R.R. 2004. Estimating fault stability and sustainable fluid pressures for underground storage of CO_2 in porous rock. *Energy*, **29**, 1445–1456.

Surlyk, F., Dons, T., Clausen, C.K. & Higham, J. 2003. Upper Cretaceous. *In:* Evans, D., Graham, C., Armour, A. & Bathurst, P. (eds) *The Millennium Atlas: Petroleum Geology of the Central and Northern North Sea*. Geological Society, London, 213–233.

Thomson & Underhill 1993. Controls on the development and evolution of structural styles in the Inner Moray Firth Basin. *In:* Parker, J.R. (ed.) *Petroleum Geology of Northwest Europe: Proceedings of the 4th Conference*. Geological Society, London, 1167–1178, http://doi.org/10.1144/0041167

White *et al.* 2002. The use of leak-off tests as means of predicting minimum *in-situ* stress. *Petroleum Geoscience*, **8**, 189–193, http://doi.org/10.1144/petgeo.8.2.189

Williams, J.D.O., Jin, M., Bentham, M., Pickup, G.E., Hannis, S.D. & Mackay, E.J. 2013. Modelling carbon dioxide storage within closed structures in the UK Bunter Sandstone Formation. *International Journal of Greenhouse Gas Control*, **18**, 38–50.

Williams, *et al.* 2014. Pressure constraints on the CO_2 storage capacity of the saline water-bearing parts of the Bunter Sandstone Formation in the UK Southern North Sea. *Petroleum Geoscience*, **20**, 155–167, http://doi.org/10.1144/petgeo2013-019

Williams, J.D.O., Fellgett, M.W., Kingdon, A. & Williamson, J.P. 2015. *In-situ* stress orientations in the UK Southern North Sea: Regional trends, deviations and detachment of the post-Zechstein stress field. *Marine and Petroleum Geology*, **67**, 769–784.

Wilson, M.P., Davies, R.J., Foulger, G.R., Julian, B.R., Styles, P., Gluyas, J.G. & Almond, S. 2015. Anthropogenic earthquakes in the UK: A national baseline prior to shale exploitation. *Marine and Petroleum Geology*, **68A**, 1–17.

Wiprut, D. & Zoback, M.D. 2000. Fault reactivation and fluid flow along a previously dormant normal fault in the northern North Sea. *Geology*, **28**, 595–598.

Worum, G., van Wees, J-D., Bada, G., van Balen, R.T., Cloetingh, S. & Pagnier, H. 2004. Slip tendency analysis as a tool to constrain fault reactivation: A numerical approach apllied to three-dimensional fault models in the Roer Valley rift system (southeast Netherlands). *Journal of Geophysical Research*, **109**, B02401.

Zanella, E. & Coward, M.P. 2003. Structural framework. *In:* Evans, D., Graham, C., Armour, A. & Bathurst, P. (eds) *The Millennium Atlas: Petroleum Geology of the Central and Northern North Sea*. Geological Society, London, 45–59.

Zoback, M.D., Moos, L.G., Mastin, L.G. & Anderson, R.N. 1985. Well bore breakouts and in situ stress. *Journal of Geophysical Research*, **90**, 5523–5530.

Zoback, M.D., Barton, C.A. *et al.* 2003. Determination of stress orientation and magnitude in deep wells. *International Journal of Rock Mechanics and Mining Sciences*, **40**, 1049–1076.